Behavior of methylammonium dipoles in $MAPbX_3$ (X = Br and I)

Sharada Govinda,[†] Bhushan. P. Kore,[†] Menno Bokdam,[‡] Pratibha Mahale,[†] Abhinav Kumar,[†] Somnath Pal,[†] Biswajit Bhattacharyya,[†] Jonathan Lahnsteiner,[‡] Georg Kresse,[‡] Cesare Franchini,[‡] Anshu Pandey[†] and D. D. Sarma[*,†]*

[†]Solid State and Structural Chemistry Unit, Indian Institute of Science, Bengaluru-560012, India

[‡]University of Vienna, Faculty of Physics and Center for Computational Materials Science, Sensengasse 8/12, 1090 Vienna, Austria

*Corresponding Author: sarma@sscu.iisc.ernet.in

ABSTRACT

Dielectric constants of $MAPbX_3$ (X = Br, I) and $CsPbBr_3$ measured in 1 kHz-1MHz range show a strong temperature dependence in and around the room temperature phases of $MAPbX_3$. In contrast, the dielectric constant of $CsPbBr_3$ is nearly temperature independent over the entire temperature range, similar to those for the low temperature phase of $MAPbX_3$. Noting the absence of any dipole containing units in $CsPbBr_3$ and the static ordering of dipoles of MA^+ units in the low temperature phase of $MAPbX_3$, the strong temperature dependence of the dielectric constant of $MAPbX_3$ in the tetragonal phase is attributed to the dipoles rotating freely with time scales much lower than probed by dielectric measurements. In order to understand the dynamics of MA^+ units, we perform extensive *ab initio* molecular dynamics simulations on $MAPbI_3$ and show that these dipoles are randomly oriented with a rotational relaxation time scale of ~ 7 ps at 300 K. Further, we probe the intriguing possibility of a transient polarization of these dipoles following a photoexcitation process that may have important consequences on the photovoltaic efficiency. We have performed pump-probe experiments to measure the second harmonic generation efficiency in $MAPbX_3$ at various delay times from about 100 fs to 1.8 ns after photoexcitation. We find no detectable second harmonic signal throughout the delay time range, which spans the relaxation time of dipoles up to the lifetime of the photoexcited electron and hole, thus ruling out the possibility of a ferroelectric state under photoexcitation.

TOC GRAPHICS

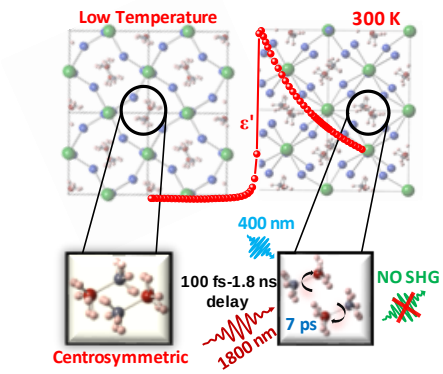

KEYWORDS: Hybrid perovskite, methylammonium dipoles, relaxation time, second harmonic generation

The interest in solution processable organic-inorganic hybrid perovskites based on lead halides has shown a huge surge as potential photovoltaic materials, with efficiency crossing 22% within a few years[1-4]. The most widely used active material is methylammonium lead iodide ($MAPbI_3$) with a near-ideal band gap of about 1.5 eV, while the bromide and chloride analogues have larger band gaps.[5-7] These compounds are characterized by the presence of the asymmetric and positively charged organic unit, methylammonium ion $(CH_3NH_3)^+$, with a permanent dipole, at the center of a lead halide cage. These perovskite materials have a low temperature orthorhombic phase and high/ room temperature cubic phase depending on the specific halide ion, with an intermediate tetragonal phase[8] that is relevant to its photovoltaic properties. Though the low-temperature structure is more or less understood,[9-10] where the methylammonium (MA^+) dipoles order in an antiferroelectric arrangement,[9] the behavior of these units and their possible roles in determining material properties in the high temperature phases have remained controversial, as discussed later. The room temperature structure of $MAPbI_3$ is, on an average, centrosymmetric– as shown by space and time averaged XRD, P-E loop, as well as Second Harmonic Generation (SHG) efficiency measurements.[11] However, this time-averaged description is consistent with many different dynamic behaviors, such as MA^+ units (i) rotating freely and independently (ii) rotating in a correlated manner, and (iii) not rotating at all, but being frozen in an uncorrelated/random manner giving rise to a glassy state. Thus, it becomes crucial to understand the time-scale of rotations of these dipoles and the extent of correlation between different MA^+ units.

Several attempts have been made in the past to address these important issues; but, unfortunately, there is no clear consensus, with claims of ordered/locally ordered as well as dynamically disordered structures of various forms having been reported in the literature. For example, there are several publications suggesting reorientation of dipoles with reported relaxation times scattered over 0.1-28 picoseconds.[8, 12-19] There are also several spectroscopic measurements that suggest dynamic disorder[20-24] in $MAPbX_3$ without the mention of any specific time-scale. Then there are also claims that the dipoles are in fact ferroelectrically ordered,[25-41] in contrast to any description based on statically or dynamically disordered dipoles. On the theoretical front, several calculations using molecular dynamics and other techniques report rotations of these dipoles with time scales of a few picoseconds.[28, 42-46] One of these calculations, however, suggests that there is a collective behavior of these dipolar MA^+ units, where they rotate as microscopic ferroelectric domains.[43] In contrast, another calculation suggests no spatial correlation between individual dipoles.[46] Another

large supercell calculation[45] shows that there is dynamical correlation present between neighboring MA^+ units in the tetragonal phase, which is mediated by the Pb-I cage and reaches its maximum at room temperature. Interestingly, in this case, the calculations are interpreted to evince an underlying long range anti-ferroelectric ordering of the MA^+ units, which is smeared out at elevated temperature.[45] This discussion makes it clear that the important issue of the behavior of dipoles on the MA^+ units, both in the ground and photoexcited states is still not clear, while the relevance of this in determining physical properties, specifically those influencing its function as the active photovoltaic material is self-evident.

Since dipoles and their behavior have a direct bearing on the dielectric constant of the material, we have performed dielectric measurements on $MAPbX_3$ with X= Br and I, as a function of temperature. In order to clearly identify the contribution from the dipoles, we have also measured dielectric properties of the related compound, $CsPbBr_3$, where the dipole on the MA^+ ion is replaced by the monopolar Cs^+ ion with no dipole on it. Therefore, a comparison of the dielectric properties of $MAPbBr_3$ and $CsPbBr_3$ is expected to make the contribution from the dipoles obvious. This comparison of the MA system with the corresponding Cs system indicates a strong temperature dependence of the dielectric constant only in $MAPbX_3$ in the tetragonal and cubic phases, and not in the low temperature orthorhombic phase. This strong temperature dependence in the two high temperature phases can be clearly attributed to dipoles rotating well below the time scale of measurement. An antiferroelectric ordering of the dipoles in the lowest temperature phase[9] is responsible for the absence of any signature of these dipoles rotating, leading to the relatively temperature independent dielectric properties, similar to what is observed for $CsPbBr_3$ over the entire temperature range. We extend the time domain to smaller time scales with the help of extensive Molecular Dynamics calculations and find that the dipoles indeed rotate in a time scale of 1 to 10 ps with little, if any, inter-site correlation.

Recently, there has also been a claim[39] of ferroelectric switching induced by photoexcitation leading to the generation of electron-hole pairs. In order to investigate the possibility of a photoabsorption induced even transient ferroelectric alignment of dipoles, we have carried out a pump-probe experiment to probe the SHG efficiency as a function of time delays after an electron-hole excitation induced by a sufficiently high energy 100 femtosecond laser pulse, down to sub-picosecond regime and up to a nanosecond which is in the order of the lifetime of the excited state.

We found no evidence of any transient ferroelectric behavior even in the excited state, suggesting other origins of its spectacular photovoltaic properties.

Dielectric constants of $MAPbBr_3$, $CsPbBr_3$ and $MAPbI_3$ were measured from about 10 K till 300 K over the frequency range of 1 kHz to 1 MHz, as shown in Figure 1 for selected frequencies. The real and imaginary part of the dielectric constant versus temperature measured on $MAPbBr_3$, $CsPbBr_3$ and $MAPbI_3$ are shown in Figure 1 at selected frequencies. The comparison of dielectric constants of $MAPbBr_3$ and $CsPbBr_3$ as a function of the temperature is shown in Figure 1a. $MAPbBr_3$ is known to have a crystallographic phase transition[8] at about 237 K from the higher temperature cubic phase to a tetragonal phase. It undergoes a further phase transition at 155 K to a second tetragonal phase and finally, it enters the low temperature orthorhombic phase on lowering the temperature below 145 K.

The dielectric constant of $MAPbBr_3$ increases monotonically as the temperature decreases from 300 K to 155 K as seen in Figure 1a, for all frequencies. A small kink is seen in the dielectric constant at ~235 K on an expanded scale, corresponding to the phase transition from cubic to tetragonal (I) phase. On lowering the temperature further, it undergoes another transition at ~ 155 K into a second tetragonal phase where the dielectric constant drops markedly. At the tetragonal to orthorhombic transition at ~142 K, the dielectric constant drops sharply and a nearly temperature independent dielectric constant is seen in the orthorhombic phase. The low frequency dielectric constant is seen to slightly increase with an increase in the temperature above 240 K; this is attributed to extrinsic contributions to the dielectric constant.

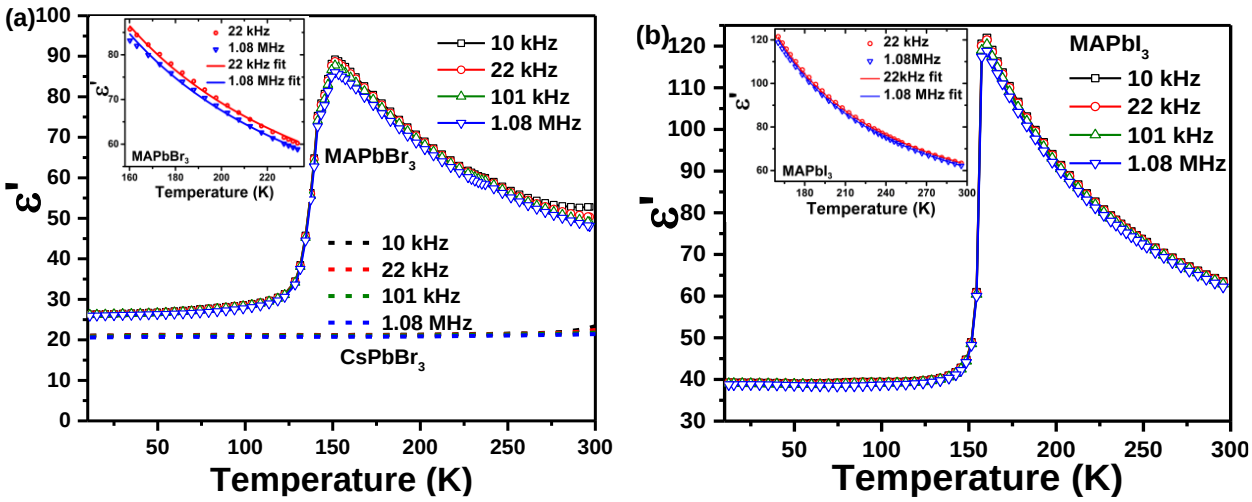

Figure 1. [a and b] Dielectric constant, ε′ versus temperature for selected frequencies measured on $MAPbBr_3$ (symbol and solid lines) and $CsPbBr_3$ (dashed lines) [panel a] and $MAPbI_3$ [panel b]. The inset in 1(a) and 1(b) show the fit to the experimental data of dielectric constant vs temperature in the tetragonal phase of $MAPbBr_3$ and $MAPbI_3$ respectively.

The dielectric constant of $CsPbBr_3$, shown as dashed lines in Figure 1a, exhibits only a slight temperature dependence increasing from 20.5 to about 22 for a temperature variation from 11 K to 300 K. Thus, the dielectric constants of $CsPbBr_3$ and $MAPbBr_3$ in the orthorhombic phase resemble each other closely in their temperature and frequency dependencies. This is not altogether surprising, since the $PbBr_3$ cage in both compounds are similar.[47] Moreover, the dipoles on MA^+ units are expected to be ordered antiferroelectrically within the orthorhombic phase.[9] Therefore, we do not expect any large thermal effects on contributions to the dielectric constant from these dipoles within the orthorhombic phase, explaining the qualitative as well as quantitative similarities of dielectric constants of these two compounds for $T < 120$ K. By the same logic, it is clear that the drastic increase of the dielectric constant for $T > 120$ K and its pronounced temperature dependence between 155 and 300 K within the tetragonal phase of interest in the case of $MAPbBr_3$, compared to that of $CsPbBr_3$ must arise from a prominent contribution of the dipoles on the MA^+ units to the dielectric constant, distinguishing $MAPbBr_3$ clearly from $CsPbBr_3$ with no dipoles. The dielectric constant of $MAPbI_3$, shown in Figure 1b, shows qualitatively similar behavior to $MAPbBr_3$. $MAPbI_3$ is orthorhombic below 162 K, with a single tetragonal phase between 162 and 331 K and a cubic phase beyond 331 K. The corresponding Cs analogue, namely, $CsPbI_3$ cannot be stabilized long enough in the relevant structure type, since it transforms readily to a non-perovskite structure type.[48] However, comparing the dielectric data of $MAPbI_3$ in Figure

1b with those of $MAPbBr_3$ and $CsPbBr_3$, we easily identify the orthorhombic phase in the low temperature as the one which is relatively less influenced by the temperature dependence of the dipoles on the MA^+ units. This can be attributed to the dipoles ordered antiferroelectrically, since there has been no evidence of a P-E loop within this low temperature phase to suggest a ferroelectric state and the crystal structure has been shown in the past to be centrosymmetric.[11] There is a clear evidence of large temperature dependent contribution from dipoles within the tetragonal phase of $MAPbI_3$ over the temperature range 162 to 300 K in Figure 1b, similar to what is found in the case of $MAPbBr_3$.

The measured temperature dependencies of the dielectric constant for $MAPbBr_3$ and $MAPbI_3$ reported here agree well with the previous reports.[20, 49-51] The comparison with the closely related $CsPbBr_3$ with no dipole, not reported earlier, makes it clear that the dipoles in $MAPbX_3$ (X = Br and I) contribute significantly to the dielectric constant in the tetragonal phase and this contribution is strongly temperature dependent, unlike in the orthorhombic phase, where the dipoles are ordered in an antiferroelectric manner, thereby suppressing any strong dynamical effects. In order to explore what kind of dynamical descriptions of these dipoles is consistent with its dielectric properties (Figures 1a and b), we examine the Debye theory of dipole relaxation that provides a description of free dipoles in a dielectric medium.

Within the Debye theory, the dielectric constant, ε', can be expressed as[8]

$$\varepsilon' = \varepsilon_\infty + \left(\frac{C}{T}\right)\frac{1}{1+\omega^2\tau^2} \qquad \text{..... (1)}$$

where ε_∞ is the high frequency dielectric constant, T is the temperature, ω the frequency of the applied electric field to measure the dielectric constant and τ(T) is the relaxation time of the dipoles. C is a system-dependent parameter containing information on the dipole moment, symmetry of the lattice etc. This constant is related to the microscopic parameters as follows[8]:

$$C = \frac{N\mu^2\eta}{3k\varepsilon_0} = \frac{n\mu^2\eta}{3Vk\varepsilon_0}$$

where the number of dipoles per unit volume N = n/V (n- number of dipoles in unit cell of volume V), μ is the dipole moment, η is the correction factor due to Lorentz local field, k the Boltzmann's constant, ε_0 the permittivity of free space. For tetragonal and cubic symmetry,[8]

$$\eta = \frac{\varepsilon_\infty + 2}{3}$$

Thus, the frequency dependency of ε' comes from the $1/(1+ \omega^2\tau^2)$ term. As is evident from the data in the Figures 1a and 1b and already discussed earlier in this work, there is very little frequency dependency of ε' in $MAPbX_3$ (X = Br and I) in the measured frequency range (kHz-MHz), except for a slight decrease with increasing frequency at the high temperature end in Figure 1a, attributed to slight extrinsic contributions. This, then, implies that $\omega\tau << 1$, as this leads to an ε' nearly independent of the frequency. Noting that the highest frequency of probe electric field employed here is 1 MHz, clearly τ is several orders of magnitude smaller than 1 μs to fulfill the above requirement. This is consistent with earlier reports[8, 12-13, 15-19] of the relaxation time of MA^+ units in the range of ps within the tetragonal phase. Thus, we may safely ignore the $\omega^2\tau^2$, thereby reducing the Debye expression (equation (1)) to

$$\varepsilon' = \varepsilon_\infty + \left(\frac{C}{T}\right) \qquad \text{..... (2)}$$

The temperature dependency of ε' arises from the 1/T term and is qualitatively consistent with the increasing value of ε' for both $MAPbBr_3$ and $MAPbI_3$ in the tetragonal phase with a decrease in temperature (Figure 1a and b). However, a detailed analysis in terms of plots of $(\varepsilon'-\varepsilon_\infty)$ as a function of 1/T for various choices of ε_∞ shows that this expression is unable to provide a proper quantitative description of the dielectric properties, suggesting a limitation intrinsic to the assumption of non-interacting dipoles in deriving equation (1). Since the dipolar interactions cannot be avoided, we account for it by replacing T with (T-T*), as has been invoked in the past literature;[20, 51] with the T* providing an energy scale of the (dipolar) interactions in close analogy to the Curie-Weiss law description of interacting paramagnetic system. This is reasonable also in the view of the fact that both systems undergo a transition to a long-range ordered state at a reasonably high ordering temperature of 144 and 162 K for X = Br and I, respectively, indicating sufficient interactions between the dipoles that would naturally be present also in the disordered paraelectric state.

In order to provide a quantitative description of the dielectric constant as a function of temperature and frequency, we need to include extrinsic contributions, since we see evidence of extrinsic contributions in terms of slight frequency dependency, for example in the case of $MAPbBr_3$ near 300 K in Figure 1a. Such extrinsic contributions are well described by Maxwell-Wagner expression[52] for ε', which when coupled with the above equation leads to

$$\varepsilon' = \varepsilon_\infty + \left(\frac{C}{T-T^*}\right) + \varepsilon_\infty^{ext} + \frac{\left(\varepsilon_s^{ext}-\varepsilon_\infty^{ext}\right)}{2}\left(1 - \frac{sinh[\beta ln(\omega\tau^{ext})]}{cosh[\beta ln(\omega\tau^{ext})]+cos(\beta\pi/2)}\right) \quad \text{..... (3)}$$

where β varies between 0 and 1 and ε_s^{ext} and ε_∞^{ext} are the static and high frequency dielectric constants contributed by external factors. The Maxwell-Wagner relaxation generally corresponds to the relaxation of grain boundaries and other such extrinsic contributions to the dielectric constant, which mostly dominate in the low frequencies and high temperatures. The dielectric data within the tetragonal phase for both $MAPbBr_3$ and $MAPbI_3$ have been fitted for the frequency range 22 kHz – 1.08 MHz using equation (3) and these are shown in insets of Figure 1a and 1b for two extreme frequencies, namely, 22 kHz and 1.08 MHz. Clearly, equation (3) provides a good description of the dielectric constants in the tetragonal phase for the compounds over the entire range of frequencies and temperatures. It is to be noted that these analyses suggest a minor contribution from the Maxwell-Wagner part arising from extrinsic parts in both cases, namely less than 0.5% for $MAPbI_3$ and 1.2% for $MAPbBr_3$ to the total dielectric constant. Various parameters in equation (3) determining the intrinsic contributions to the dielectric constants, obtained from the fit are given in Table I.

Table I: Parameters obtained from fitting the dielectric data in the tetragonal phase.

	$MAPbI_3$	$MAPbBr_3$
C (K)	9221	7080
ε_∞	22	20
T* (K)	66.2	50.4
μ (Cm)	10.23×10^{-30}	8.51×10^{-30}

The constant, C, obtained from fits to our dielectric data is very similar to that obtained by dielectric measurement[8] at 90 GHz for both $MAPbBr_3$ and $MAPbI_3$. Unit cell volume reported in Ref[8] has been used to estimate the dipole moment. The ε_∞ value obtained by the fits are in the same range as the ε_∞ values reported by similar measurements, for example[8, 20] between ~23 – 29 for $MAPbI_3$ and ~26 – 29 for $MAPbBr_3$. Thus, we see that the dipoles on the MA^+ units can be described as essentially free dipoles with relaxation time much shorter than the probing time scale down to μs, thereby establishing the intrinsic paraelectric state of the dipoles in the tetragonal phase.

In order to probe the dynamical behavior of individual dipoles down to a much shorter time scale and to obtain a microscopic understanding of dynamical or local correlations, if any, between dipoles beyond what can be probed by any type of dielectric measurements, we have performed large scale ab-initio Molecular Dynamics (MD) calculations at finite temperatures. For these calculations we have constructed super cells of $MAPbI_3$ containing n x n x n unit cells with n=2, 4 and 6. From the trajectory, we extract the orientation of all MA^+ units. We define the time-dependent molecular polarization as the vectorial average of all dipole moments of the molecules

$$P_{mol}(t) = \left|\frac{1}{N}\sum_{i=1}^{N}\overrightarrow{p_i}(t)\right| \qquad \ldots (4)$$

Since the MA^+ is chemically decoupled from the Pb-I framework[7], it is a reasonable assumption that the time evolution of the intrinsic dipole moment vector ($\hat{p}_i$) of each molecule is largely controlled by its direction, while the magnitude of the dipole moment remains essentially unchanged.

In order to understand the behavior of these dipoles within the tetragonal phase, we first started with a fully ferroelectrically polarized structure by aligning all dipoles as the starting of our MD calculations at 300 K; the time evolution of the molecular polarization of this aligned structure, A, is shown in Figure 2 by the red dash-dot line. We find that the initial, fully polarized value of unity for $\bar{P}_{mol}(t = 0)$ rapidly decreases, to approach a depolarized state with the first ~ 20 ps of the MD trajectory at 300 K for the 64-unit cell (A) structure is only used to break down the polarized state. This rapid depolarization of a starting polarized state within the MD provides a clear argument against a ferroelectric state being present within the tetragonal phase. It also suggests that the opposite limit of a totally randomized dipoles is a better starting point for the MD steps, so that computationally heavy MD calculations over a large time window are not required only to equilibrate a starting structure far from the equilibrium.

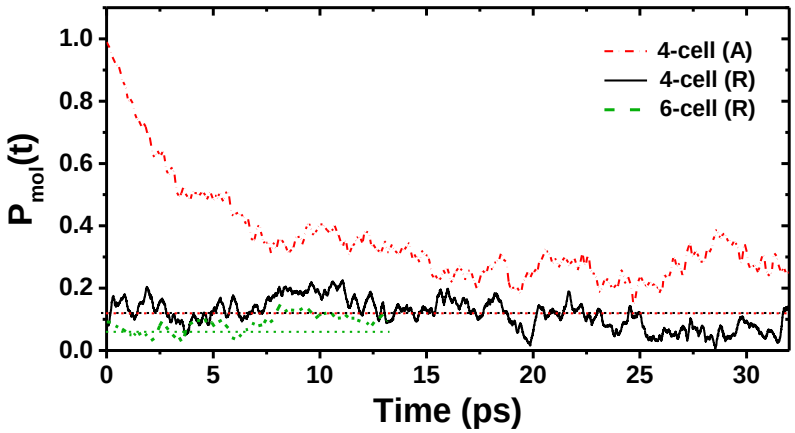

Figure 2. Molecular polarization $P_{mol}(t)$ in the 64- and 216- unit cell, called 4-cell and 6-cell respectively, at 300 K starting from an unpolarized-random (R) structure and from a polarized-aligned (A) starting structure. Average values for independent-random dipoles for the same system size have been indicated by the dashed lines.

Therefore, for all subsequent calculations, all molecules in the super cells have been randomly rotated over three axes to generate an unbiased, not polarized starting structure (R) with 64- and 216-unit cells. After initial equilibration time, both calculations show a fluctuating behavior with variance (σ^2_{mol}) around a mean value $\bar{P}_{mol}(t)$. This mean value depends on the size of the super cell employed, as evident in Figure 2. In order to understand the significance of these mean values and to serve as a reference, we have calculated $P_{mol}(t)$ for random uncorrelated dipoles. This is calculated by assigning a new random orientation to the dipoles at every time step and determining values for ($\bar{P}_{rand}, \sigma^2_{rand}$). All these results are compiled in Table II and the $\bar{P}_{rand}$ levels are shown as dashed lines in Figure 2. The average total molecular polarization ($\bar{P}_{mol}$) from the MD simulation does not differ that much from $\bar{P}_{rand}$, thereby establishing that the equilibrated structure is as effectively randomized as possible within a given system size. It is also seen that with increasing super cell size, $\bar{P}_{mol}$ decreases systematically. Extrapolating this behavior to even larger super cells indicates the absence of any macroscopic molecular spontaneous polarization at 300 K. Figure 2 shows that the dipoles are dynamic in nature, fluctuating perceptibly as evidenced by the instantaneous deviations of the $P_{mol}(t)$ from $\bar{P}_{mol}$ at various time steps. This is also reflected in the fact that the variance in the MD is about one order larger than in the random reference system (see Table II). We have estimated the typical relaxation time τ_{mol} of these dipoles from their autocorrelation functions averaged over all dipoles and found it to be ~ 7 ps at 300 K. Lowering or raising the temperature within the tetragonal phase lowers or raises τ_{mol} and σ_{mol}, respectively.

The value of $\bar{P}_{mol}$ is, however, almost unaffected. The ps rotational mobility explains why these dipoles, when probed for their dielectric properties with a frequency of MHz, appear to be essentially free dipoles with no perceivable frequency dependence and explains the absence of simple 1/T dependence in Ref [8] where 90 GHz field was used.

Table II. Average molecular polarization ($\bar{P}_{mol}$), the variance of $\bar{P}_{mol}(t)$ (σ^2_{mol}) and the relaxation time (τ_{mol}) for a n-cell at 300 K staring from a polarized-aligned (A) and an unpolarized-random (R) structure. The last two columns list the reference values for uncorrelated random dipoles.

System	$\bar{P}_{mol}$	σ^2_{mol}	$\tau_{mol}(ps)$	$\bar{P}_{rand}$	σ^2_{rand}
2 × 2 × 2 (R)	0.31	0.11	7	0.33	$2x10^{-2}$
4 × 4 × 4 (A)	0.27	0.05	8	0.12	$2x10^{-3}$
4 × 4 × 4 (R)	0.15	0.03	7	0.12	$2x10^{-3}$
6 × 6 × 6 (R)	0.07	0.02	5	0.06	$7x10^{-4}$

Though above results establish a free dipole-like behavior of MA^+ molecules in the ground state for all practical time-scales of relevance for its photovoltaic properties, it does not eliminate the possibility of local ferroelectric ordering of these dipoles following the creation of the photoexcited state with an electron and a hole. The presence of additional charge carriers in the system, such as after a photoexcitation, can alter the behaviour of dipoles significantly. It is conceivable that the electron and the hole, particularly with a small excitonic binding energy, migrate to opposite ends of the dipole, thereby inhibiting the rotational dynamics and enhancing the possibility of a dipole ordering at the same time. This is indeed an interesting possibility that merits a careful investigation, which appears feasible since there are already claims of photoinduced ferroelectric switching in such materials,[39] indicative of a strong coupling between the exciton and the local polarization field. If true, such effects can significantly alter photovoltaic properties of the material by generating an internal local field during the lifetime of the excited electrons and holes. In order to examine this possibility, one necessarily needs a time-resolved experiment, capable of probing the system many times over within the photoexcited state lifetime, which is in the range of ns. Therefore, we have performed pump-probe experiments to probe the possibility of a transient ferroelectric state generated by the primary step of an electron-hole excitation.

We have performed pump-probe experiments on polycrystalline pellets of $MAPbI_3$, $MAPbBr_3$ and $CsPbBr_3$ using a pump of 400 nm (3.1 eV) which was obtained by frequency doubling of a primary source at 800 nm (1.55 eV) for the photoexcitation step. A probe of 1800 nm (0.69 eV) with various delay times was used in an attempt to excite SHG signals at 900 nm (1.38 eV), as a signature of a non-centrosymmetric structure, which is a necessary condition for any (even transient) ferroelectric state. The choice of the pump wavelength is of course dictated by the requirement that it is more energetic than the bandgaps[5, 53-54] 1.51, 2.2, and 2.25 eV of $MAPbI_3$, $MAPbBr_3$ and $CsPbBr_3$, respectively. The probe wavelength was carefully chosen so as to avoid any absorption of the SHG signal, by keeping it energetically below the bandgap for each case.

The time delay for the probe was varied from 100 fs to 1.8 ns; spectra recorded for a few selected values of the time delay are shown in Figures 3a, b and c for $MAPbI_3$, $MAPbBr_3$ and $CsPbBr_3$ samples, respectively. The normal SHG spectrum of urea, a common standard for SHG, recorded at the same laser power is shown in each panel for comparison. It can be seen that the spectra of samples at each delay time overlap. In $MAPbI_3$, the decaying tail of intense photoluminescence (PL) at ~ 805 nm is observed over the entire range of the plot, while in $MAPbBr_3$ and $CsPbBr_3$, a gently sloping background of much lower intensity is observed, which arises from the tail of the primary source at 800 nm used to generate the 400 nm pump. However, it is clear that in all three cases, there is essentially no SHG signal that should appear, if present, as a peak at around 900 nm. In order to be more quantitative, we have analyzed the recorded signal after removing background contributions, including the tail of the PL signal in the case of $MAPbI_3$ (see Supporting Information), to estimate the upper limit of any possible signal at the second harmonic for each delay time for all three samples. The relative SHG efficiency has been calculated as the ratio of area under the Gaussian of SHG signal of sample to that of urea, and is plotted as a function of the delay time in Figure 4.

In order to understand the influence of the primary photoexcitation on the efficiency of SHG in these materials, we have indicated with a dashed line in each of the three panels the estimated upper limit of any relative SHG efficiency from these compounds in absence of any photoexcitation. The results for $CsPbBr_3$, shown in the lowest panel of Figure 4, provides us with an estimate of limits of significance of SHG signal extracted from our experiments, since, in absence of any permanent dipolar unit, $CsPbBr_3$ is centrosymmetric in its ground state and

therefore, cannot have any SHG signal in absence of any photoexcitation. While it is not impossible, it is improbable that the photoexcited state of $CsPbBr_3$ would adopt a non-centrosymmetric structure. This is clearly supported by the measured SHG signal of the photoexcited $CsPbBr_3$ with various time delays in the lowest panel of Figure 4, exhibiting, random, insignificant fluctuations around the base level (dashed line) defined by the SHG signal intensity from the ground state $CsPbBr_3$.

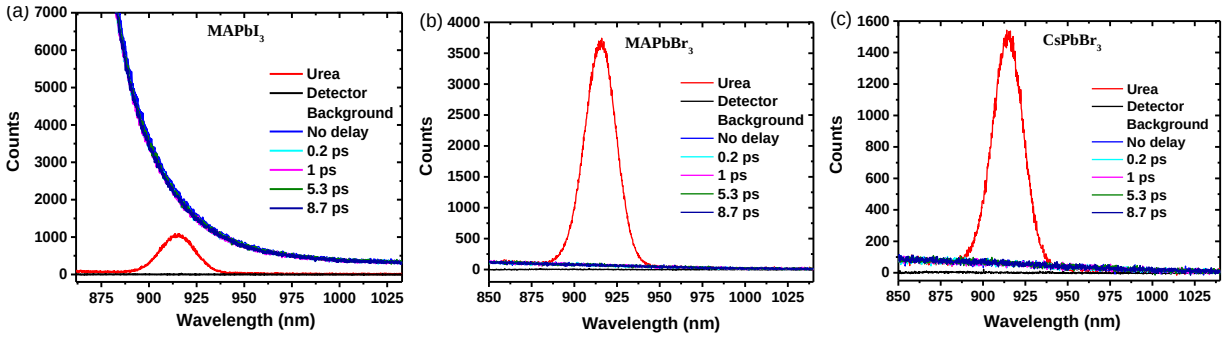

Figure 3. Spectra of second harmonic generated at 900 nm with incident 1800 nm laser measured on (a) $MAPbI_3$ and urea with pump power 2.84 mW, (b) $MAPbBr_3$ with pump power 2.62 mW and (c) $CsPbBr_3$ with pump power 2.60 mW at a few selected delay times indicated in the legend. It can be seen that all the spectra at different delay times overlap.

This base level, essentially defining the zero of the SHG signal, is essentially determined by the detector background. Comparing the data shown in the other two panels for $MAPbBr_3$ and $MAPbI_3$; it becomes clear at once that these also exhibit no detectable SHG activities either in the ground states or in the photoexcited state at any instant of time between the photoexcitation and the lifetime of the photoexcited state. It is important to note that we have explored over the delay time spanning four decades; specifically, the longest delay time recorded here is of the order of the lifetime of the excited state. Moreover, at this end the delay time employed is more than two orders of magnitude larger than the dipole rotational time-scale of ~ 7 ps.

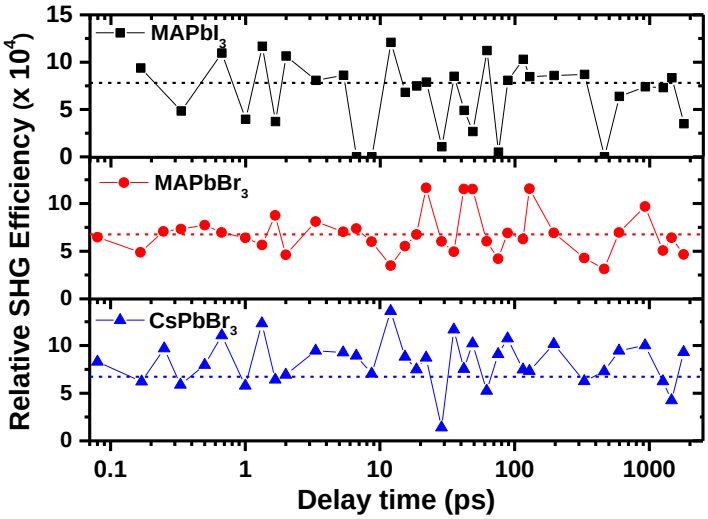

Figure 4. SHG efficiency of $MAPbI_3$, $MAPbBr_3$ and $CsPbBr_3$ with respect to urea plotted against delay time between 400 nm pump and 1800 nm probe. The dashed lines drawn for reference in each panel represent the average SHG efficiency calculated for spectra before the arrival of the pump pulse. The pump power were 2.84, 2.62 and 2.60 mW respectively for the three samples.

Therefore, if the creation of electron-hole pair were to induce reorientations of the dipoles to give rise to a locally polar state, there would be enough time for the dipoles to achieve such a "ferroelectric" excited state within the time-scale of the probe. Therefore, the complete absence of any SHG activity at any time point over this wide window of delay time is a strong evidence for the absence of any collective orientation of dipoles in the photoexcited state.

In conclusion, careful dielectric measurements comparing $CsPbBr_3$ with $MAPbX_3$ (X = Br and I), suggest that the dipoles on MA^+ units behave like free dipoles in the time-scale of measurements down to 1μs within the tetragonal phase, though they are ordered in the low temperature orthorhombic phase. Extending our investigation down to ps regime with the help of extensive molecular dynamics calculations, we find that the characteristic rotational time-scale of these dipoles is ~ 7 ps in the tetragonal phase and the dipoles undergo rotational relaxation with little correlation between them. Time resolved pump-probe experiments over four decades of time delays, from < 100 fs to > 1 ns, establish that the photoexcited state does not lead to a transient polarized state at any stage within the lifetime of the electron-hole excited state.

Experimental Section:

Synthesis. $MAPbI_3$ was synthesized according to the methods outlined in earlier report[5] with slight modifications. Polycrystalline $MAPbI_3$ was prepared from a solution made of MAI and PbI_2 in γ-butyrolactone. $MAPbI_3$ powder sample was synthesized according to the methods outlined in earlier reports with little modifications 1M solution of MAI and PbI_2 (99%, Sigma Aldrich) was heated with constant stirring for 1 hour. This solution was then drop cast on glass slides at 100°C. After 15-20 minutes, when the solvent evaporated completely, and small crystals of $MAPbI_3$ were scratched off from the glass slides and then ground into powder and stored in vacuum.

$MAPbBr_3$ was prepared[55] from a 1M solution of MABr and $PbBr_2$ (99%, Alfa Aeser) in N,N-dimethyl formamine (DMF). This solution was stirred constantly at room temperature for 1 hour and then drop cast on glass slides at 120°C. After the solvent evaporated completely in about 15-20 minutes, the orange powder and small crystals of $MAPbBr_3$ were collected and powdered and stored in vacuum.

$CsPbBr_3$ was prepared by a method reported in Ref [56]with some modifications using a 0.5 M solution of CsBr and $PbBr_2$ in DMSO. This solution was stirred constantly at 80 ^oC for 1 hour and then drop cast on glass slides at 185 °C. After all the solvent evaporated, the powder of $CsPbBr_3$ was collected and stored in vacuum.

Synthesis of precursors MAI[5] and MABr[57]: . MAI was prepared by reacting Methylamine (40% in water) with hydroiodic acid at 0 °C for two hours. The reaction mixture was distilled to obtain MAI as precipitate. This was washed with diethyl ether several times to remove unreacted HI and dried and stored in vacuum. MABr was prepared similarly by reacting methylamine with HBr.

Powder X-Ray Diffraction. All samples were prepared just before the experiments and the powder XRD pattern collected in order to check the purity of the samples. Typical powder XRD patterns of each sample recorded before experiment are shown in Figure S1 in Supporting Information.

Dielectric measurements. Polycrystalline samples of $MAPbI_3$, $MAPbBr_3$ and $CsPbBr_3$ was ground to fine powder in a mortar and pressed into pellets of 6 mm diameter in a steel die with a pressure of 0.15 kN/cm^2. The pellets were annealed at ~ 90 °C for 1 hour in Argon gas flow. The XRD pattern of the pellet was checked after the pellet cooled down to the room temperature. Silver paste was used to make electrodes on each face of flat pieces of the pellet (about 0.5 mm thick).

Dielectric measurements were performed with the sample inside a closed-cycle He cryostat (Sumitomo) using Keysight E4990A Impedance Analyser. Capacitance-loss (Cp-D) measurements were performed at each temperature in the frequency range 20 Hz- 2 MHz with applied peak voltage of 0.5 V. The data was collected in cooling cycle from 300 K to 10 K with a step of 5 K otherwise and 3 K near phase transitions. The sample was cooled with a ramp rate of 0.5 K/minute (controlled using Temperature Controller - Lakeshore 332) between two temperature points and allowed to stabilize for sufficient time. Data was also collected during ramping and measurements made during ramping matched very well with the measurements after temperature stabilization. Cp-D measurements were also done while heating the sample from 10 K to 300 K and it was found that it matches well with the cooling cycle, except for some hysteresis in the transition temperature. Further, the measurements were also performed with a DC voltage applied at various temperatures and it was found that these matched exactly with the data with zero voltage, hence ruling out the possibility of contribution due to space charge and similar effect.

Second Harmonic Generation. Pump-probe experiment to measure SHG was performed using a 100 fs pump of wavelength 400 nm and probe of wavelength 1800 nm. The details of the experimental set-up is described elsewhere.[11] Polycrystalline samples of $MAPbI_3$, $MAPbBr_3$, $CsPbBr_3$ and urea were ground into fine powder and pressed into pellets for this measurement. A time delay stage was used to change the delay between the pump and probe pulses. The second harmonic spectra recorded by a cooled CCD (Andor IDUS) in the range 850-1050 nm. SHG was measured on urea, a standard sample used for SHG, before each sample to confirm that SHG is indeed observed. Probe power used was between 1.3 – 1.8 mW for all samples, focused at a spot of diameter 0.95mm. The pump power was ~ 1.5 mW and 2.5 mW for two different measurements on each sample, with a spot of diameter 4.8 mm.

Computational Method:

For the first-principles molecular dynamics calculations we use a plane-wave basis and the projector augmented wave (PAW) method[58] as implemented in the VASP code.[59-61] The PBEsol[62] functional is used. Relatively shallow pseudo-potentials are used, for Pb the ($6s^26p^2$), for I the ($5s^25p^5$), for C the ($2s^22p^2$) and for N the ($2s^22p^3$) orbitals are included in the valence. This makes it possible to set a relatively low energy cut-off of 250 eV to form the plane-wave basis. Gaussian smearing with σ = 0.05 eV is used to broaden the one-electron levels. The Brillouin zone is

sampled by the Γ point only for the large 4- and 6-cell and by the Γ and R point for the 2-cell. The Kohn-Sham orbitals are updated in the self-consistency cycle until an energy convergence of 10^{-4} eV is obtained. A Langevin thermostat[63] is applied to simulate a canonical ensemble. The trajectory is formed by propagating the structure with the calculated Hellmann-Feynman forces with time steps of 0.7/2.0/3.0 fs and increased hydrogen masses of 2/4/8 a.u. for the 2/4/6-cell, respectively. The hydrogen masses are increased to allow for a larger time step for the large cell-sizes. Additionally in the 6-cell the Pb and I masses have been decreased to 20 a.u. Super cells (n × n × n, with n = 2, 4, 6) were constructed out of pseudo-cubic unit cells (12 atoms) with experimental lattice constants (a, b = 6.3115 Å, c = 6.3161 Å)[25] as described in Ref.[7] In the super cell all atoms were allowed to move while keeping the lattice vectors fixed. The relaxation time is obtained by calculating the average auto correlation function of all molecules. More details can be found in Ref.[45]

AUTHOR INFORMATION

Corresponding Author

*Email: sarma@sscu.iisc.ernet.in

ACKNOWLEDGEMENT

The authors thank Department of Science and Technology, Government of India for support, Mr. Guru Pratheep. R. for help with SHG measurement. SG thanks Dr. Sumanta Mukherjee for useful discussions and acknowledges CSIR for a student fellowship. BPK acknowledge UGC, India for a D.S. Kothari Postdoctoral Fellowship. MB and JL acknowledge funding by the Austrian Science Fund (FWF): P 30316-N27.

SUPPORTING INFORMATION

Additional figures and analysis as described in text.

REFERENCES:

1. Bi, D.; Tress, W.; Dar, M. I.; Gao, P.; Luo, J.; Renevier, C.; Schenk, K.; Abate, A.; Giordano, F.; Correa Baena, J.-P.; Decoppet, J.-D.; Zakeeruddin, S. M.; Nazeeruddin, M. K.; Grätzel, M.; Hagfeldt, A. Efficient luminescent solar cells based on tailored mixed-cation perovskites. *Sci. Adv.* **2016,** *2* (1).
2. McMeekin, D. P.; Sadoughi, G.; Rehman, W.; Eperon, G. E.; Saliba, M.; Hörantner, M. T.; Haghighirad, A.; Sakai, N.; Korte, L.; Rech, B.; Johnston, M. B.; Herz, L. M.; Snaith, H. J. A mixed-cation lead mixed-halide perovskite absorber for tandem solar cells. *Science* **2016,** *351* (6269), 151.
3. Saliba, M.; Matsui, T.; Seo, J.-Y.; Domanski, K.; Correa-Baena, J.-P.; Nazeeruddin, M. K.; Zakeeruddin, S. M.; Tress, W.; Abate, A.; Hagfeldt, A.; Gratzel, M. Cesium-containing triple cation perovskite solar cells: improved stability, reproducibility and high efficiency. Energy Environ. Sci. **2016,** *9* (6), 1989-1997.
4. Yoon, H.; Kang, S. M.; Lee, J.-K.; Choi, M. Hysteresis-free low-temperature-processed planar perovskite solar cells with 19.1% efficiency. Energy Environ. Sci. **2016,** *9* (7), 2262-2266.
5. Baikie, T.; Fang, Y.; Kadro, J. M.; Schreyer, M.; Wei, F.; Mhaisalkar, S. G.; Graetzel, M.; White, T. J. Synthesis and crystal chemistry of the hybrid perovskite $(CH_3NH_3)PbI_3$ for solid-state sensitised solar cell applications. *J.Mater. Chem. A* **2013,** *1* (18), 5628-5641.
6. Butler, K. T.; Frost, J. M.; Walsh, A. Band alignment of the hybrid halide perovskites $CH_3NH_3PbCl_3$, $CH_3NH_3PbBr_3$ and $CH_3NH_3PbI_3$. *Mater. Horiz.* **2015,** *2* (2), 228-231.
7. Bokdam, M.; Sander, T.; Stroppa, A.; Picozzi, S.; Sarma, D. D.; Franchini, C.; Kresse, G. Role of Polar Phonons in the Photo Excited State of Metal Halide Perovskites. *Sci. Rep.* **2016,** *6*, 28618.
8. Poglitsch, A.; Weber, D. Dynamic disorder in methylammoniumtrihalogenoplumbates (II) observed by millimeter-wave spectroscopy. *J. Chem. Phys.* **1987,** *87* (11), 6373-6378.
9. Swainson, I. P.; Hammond, R. P.; Soullière, C.; Knop, O.; Massa, W. Phase transitions in the perovskite methylammonium lead bromide, $CH_3ND_3PbBr_3$. *J. Solid State Chem.* **2003,** *176* (1), 97-104.
10. Chi, L.; Swainson, I.; Cranswick, L.; Her, J.-H.; Stephens, P.; Knop, O. The ordered phase of methylammonium lead chloride $CH_3ND_3PbCl_3$. *J. Solid State Chem* **2005,** *178* (5), 1376-1385.
11. G, S.; Mahale, P.; Kore, B. P.; Mukherjee, S.; Pavan, M. S.; De, C.; Ghara, S.; Sundaresan, A.; Pandey, A.; Guru Row, T. N.; Sarma, D. D. Is $CH_3NH_3PbI_3$ Polar? *J. Phys. Chem. Lett.* **2016,** *7* (13), 2412-2419.
12. Wasylishen, R. E.; Knop, O.; Macdonald, J. B. Cation rotation in methylammonium lead halides. *Solid State Commun.* **1985,** *56* (7), 581-582.
13. Knop, O.; Wasylishen, R. E.; White, M. A.; Cameron, T. S.; Oort, M. J. M. V. Alkylammonium lead halides. Part 2. $CH_3NH_3PbX_3$ (X = Cl, Br, I) perovskites: cuboctahedral halide cages with isotropic cation reorientation. *Can. J. Chem.* **1990,** *68* (3), 412-422.
14. Onoda-Yamamuro, N.; Matsuo, T.; Suga, H. Calorimetric and IR spectroscopic studies of phase transitions in methylammonium trihalogenoplumbates (II)†. *J. Phys. Chem. Solids* **1990,** *51* (12), 1383-1395.
15. Bakulin, A. A.; Selig, O.; Bakker, H. J.; Rezus, Y. L. A.; Müller, C.; Glaser, T.; Lovrincic, R.; Sun, Z.; Chen, Z.; Walsh, A.; Frost, J. M.; Jansen, T. L. C. Real-Time Observation of Organic Cation Reorientation in Methylammonium Lead Iodide Perovskites. *J. Phys. Chem. Lett.* **2015,** *6* (18), 3663-3669.

16. Chen, T.; Foley, B. J.; Ipek, B.; Tyagi, M.; Copley, J. R. D.; Brown, C. M.; Choi, J. J.; Lee, S.-H. Rotational dynamics of organic cations in the $CH_3NH_3PbI_3$ perovskite. *Phys. Chem. Chem. Phys.* **2015,** *17* (46), 31278-31286.
17. Leguy, A. M. A.; Frost, J. M.; McMahon, A. P.; Sakai, V. G.; Kockelmann, W.; Law, C.; Li, X.; Foglia, F.; Walsh, A.; O/'Regan, B. C.; Nelson, J.; Cabral, J. T.; Barnes, P. R. F. The dynamics of methylammonium ions in hybrid organic-inorganic perovskite solar cells. *Nat. Commun.* **2015,** *6*.
18. Létoublon, A.; Paofai, S.; Rufflé, B.; Bourges, P.; Hehlen, B.; Michel, T.; Ecolivet, C.; Durand, O.; Cordier, S.; Katan, C.; Even, J. Elastic Constants, Optical Phonons, and Molecular Relaxations in the High Temperature Plastic Phase of the $CH_3NH_3PbBr_3$ Hybrid Perovskite. *J. Phys. Chem. Lett.* **2016,** *7* (19), 3776-3784.
19. Selig, O.; Sadhanala, A.; Müller, C.; Lovrincic, R.; Chen, Z.; Rezus, Y. L. A.; Frost, J. M.; Jansen, T. L. C.; Bakulin, A. A. Organic Cation Rotation and Immobilization in Pure and Mixed Methylammonium Lead-Halide Perovskites. *J. Am. Chem. Soc.* **2017,** *139* (11), 4068-4074.
20. Onoda-Yamamuro, N.; Matsuo, T.; Suga, H. Dielectric study of $CH_3NH_3PbX_3$ (X = Cl, Br, I). *J. Phys. Chem. Solids* **1992,** *53* (7), 935-939.
21. Chen, H.-W.; Sakai, N.; Ikegami, M.; Miyasaka, T. Emergence of Hysteresis and Transient Ferroelectric Response in Organo-Lead Halide Perovskite Solar Cells. *J. Phys. Chem. Lett.* **2015,** *6* (1), 164-169.
22. Quarti, C.; Grancini, G.; Mosconi, E.; Bruno, P.; Ball, J. M.; Lee, M. M.; Snaith, H. J.; Petrozza, A.; Angelis, F. D. The Raman Spectrum of the $CH_3NH_3PbI_3$ Hybrid Perovskite: Interplay of Theory and Experiment. *J. Phys. Chem. Lett.* **2014,** *5* (2), 279-284.
23. Wei, J.; Zhao, Y.; Li, H.; Li, G.; Pan, J.; Xu, D.; Zhao, Q.; Yu, D. Hysteresis Analysis Based on the Ferroelectric Effect in Hybrid Perovskite Solar Cells. *J. Phys. Chem. Lett.* **2014,** *5* (21), 3937-3945.
24. Brivio, F.; Frost, J. M.; Skelton, J. M.; Jackson, A. J.; Weber, O. J.; Weller, M. T.; Goñi, A. R.; Leguy, A. M. A.; Barnes, P. R. F.; Walsh, A. Lattice dynamics and vibrational spectra of the orthorhombic, tetragonal, and cubic phases of methylammonium lead iodide. *Phys. Rev. B* **2015,** *92* (14), 144308.
25. Stoumpos, C. C.; Malliakas, C. D.; Kanatzidis, M. G. Semiconducting Tin and Lead Iodide Perovskites with Organic Cations: Phase Transitions, High Mobilities, and Near-Infrared Photoluminescent Properties. *Inorg. Chem.* **2013,** *52* (15), 9019-9038.
26. Frost, J. M.; Butler, K. T.; Brivio, F.; Hendon, C. H.; van Schilfgaarde, M.; Walsh, A. Atomistic Origins of High-Performance in Hybrid Halide Perovskite Solar Cells. *Nano Lett.* **2014,** *14* (5), 2584-2590.
27. Kutes, Y.; Ye, L.; Zhou, Y.; Pang, S.; Huey, B. D.; Padture, N. P. Direct Observation of Ferroelectric Domains in Solution-Processed $CH_3NH_3PbI_3$ Perovskite Thin Films. *J. Phys. Chem. Lett.* **2014,** *5* (19), 3335-3339.
28. Quarti, C.; Mosconi, E.; De Angelis, F. Interplay of Orientational Order and Electronic Structure in Methylammonium Lead Iodide: Implications for Solar Cell Operation. *Chem. Mater.* **2014,** *26* (22), 6557-6569.
29. Zheng, F.; Takenaka, H.; Wang, F.; Koocher, N. Z.; Rappe, A. M. First-Principles Calculation of the Bulk Photovoltaic Effect in $CH_3NH_3PbI_3$ and $CH_3NH_3PbI_{3-x}Cl_x$. *J. Phys. Chem. Lett.* **2015,** *6* (1), 31-37.
30. Chen, B.; Shi, J.; Zheng, X.; Zhou, Y.; Zhu, K.; Priya, S. Ferroelectric solar cells based on inorganic-organic hybrid perovskites. *J. Mater. Chem. A* **2015,** *3* (15), 7699-7705.

31. Dang, Y.; Liu, Y.; Sun, Y.; Yuan, D.; Liu, X.; Lu, W.; Liu, G.; Xia, H.; Tao, X. Bulk crystal growth of hybrid perovskite material $CH_3NH_3PbI_3$. *CrystEngComm* **2015,** *17* (3), 665-670.
32. Kim, H.-S.; Kim, S. K.; Kim, B. J.; Shin, K.-S.; Gupta, M. K.; Jung, H. S.; Kim, S.-W.; Park, N.-G. Ferroelectric Polarization in $CH_3NH_3PbI_3$ Perovskite. *J. Phys. Chem. Lett.* **2015,** *6* (9), 1729-1735.
33. Liu, S.; Zheng, F.; Koocher, N. Z.; Takenaka, H.; Wang, F.; Rappe, A. M. Ferroelectric Domain Wall Induced Band Gap Reduction and Charge Separation in Organometal Halide Perovskites. *J. Phys. Chem. Lett* **2015,** *6* (4), 693-699.
34. Rashkeev, S. N.; El-Mellouhi, F.; Kais, S.; Alharbi, F. H. Domain Walls Conductivity in Hybrid Organometallic Perovskites and Their Essential Role in $CH_3NH_3PbI_3$ Solar Cell High Performance. *Sci. Rep.* **2015,** *5*, 11467.
35. Stroppa, A.; Quarti, C.; De Angelis, F.; Picozzi, S. Ferroelectric Polarization of $CH_3NH_3PbI_3$: A Detailed Study Based on Density Functional Theory and Symmetry Mode Analysis. *J. Phys. Chem. Lett* **2015,** *6* (12), 2223-2231.
36. Seol, D.; Han, G. S.; Bae, C.; Shin, H.; Jung, H. S.; Kim, Y. Screening effect on photovoltaic performance in ferroelectric $CH_3NH_3PbI_3$ perovskite thin films. *J. Mater. Chem. A* **2015,** *3* (40), 20352-20358.
37. Zhao, P.; Xu, J.; Ma, C.; Ren, W.; Wang, L.; Bian, L.; Chang, A. Spontaneous polarization behaviors in hybrid halide perovskite film. *Scr.Mater.* **2015,** *102*, 51-54.
38. Hermes, I. M.; Bretschneider, S. A.; Bergmann, V. W.; Li, D.; Klasen, A.; Mars, J.; Tremel, W.; Laquai, F.; Butt, H.-J.; Mezger, M.; Berger, R.; Rodriguez, B. J.; Weber, S. A. L. Ferroelastic Fingerprints in Methylammonium Lead Iodide Perovskite. *J. Phys.Chem. C* **2016,** *120* (10), 5724-5731.
39. Wang, P.; Zhao, J.; Wei, L.; Zhu, Q.; Xie, S.; Liu, J.; Meng, X.; Li, J. Photo-induced ferroelectric switching in perovskite $CH_3NH_3PbI_3$ films. *Nanoscale* **2017,** *9* (11), 3806-3817.
40. Rakita, Y.; Bar-Elli, O.; Meirzadeh, E.; Kaslasi, H.; Peleg, Y.; Hodes, G.; Lubomirsky, I.; Oron, D.; Ehre, D.; Cahen, D. Tetragonal $CH_3NH_3PbI_3$ is ferroelectric. *Proc. Natl. Acad. Sci.* **2017**.
41. Rohm, H.; Leonhard, T.; Hoffmann, M. J.; Colsmann, A. Ferroelectric domains in methylammonium lead iodide perovskite thin-films. *Energy Environ. Sci.* **2017,** *10* (4), 950-955.
42. Carignano, M. A.; Kachmar, A.; Hutter, J. Thermal Effects on $CH_3NH_3PbI_3$ Perovskite from Ab Initio Molecular Dynamics Simulations. *J. Phys. Chem. C* **2015,** *119* (17), 8991-8997.
43. Goehry, C.; Nemnes, G. A.; Manolescu, A. Collective Behavior of Molecular Dipoles in $CH_3NH_3PbI_3$. *J. Phys. Chem. C* **2015,** *119* (34), 19674-19680.
44. Mattoni, A.; Filippetti, A.; Saba, M. I.; Delugas, P. Methylammonium Rotational Dynamics in Lead Halide Perovskite by Classical Molecular Dynamics: The Role of Temperature. *J. Phys. Chem. C* **2015,** *119* (30), 17421-17428.
45. Lahnsteiner, J.; Kresse, G.; Kumar, A.; Sarma, D. D.; Franchini, C.; Bokdam, M. Room-temperature dynamic correlation between methylammonium molecules in lead-iodine based perovskites: An ab initio molecular dynamics perspective. *Phys.Rev.B* **2016,** *94* (21), 214114.
46. Meloni, S.; Moehl, T.; Tress, W.; Franckevičius, M.; Saliba, M.; Lee, Y. H.; Gao, P.; Nazeeruddin, M. K.; Zakeeruddin, S. M.; Rothlisberger, U.; Graetzel, M. Ionic polarization-induced current–voltage hysteresis in $CH_3NH_3PbX_3$ perovskite solar cells. *Nat. Commun.* **2016,** *7*, 10334.
47. Kulbak, M.; Gupta, S.; Kedem, N.; Levine, I.; Bendikov, T.; Hodes, G.; Cahen, D. Cesium Enhances Long-Term Stability of Lead Bromide Perovskite-Based Solar Cells. *J. Phys. Chem. Lett.* **2016,** *7* (1), 167-172.

48. Eperon, G. E.; Paterno, G. M.; Sutton, R. J.; Zampetti, A.; Haghighirad, A. A.; Cacialli, F.; Snaith, H. J. Inorganic caesium lead iodide perovskite solar cells. *J. Mater. Chem. A* **2015,** *3* (39), 19688-19695.
49. Gesi, K. Effect of hydrostatic pressure on the structural phase transitions in $CH_3NH_3PbX_3$ (X = Cl, Br, I). *Ferroelectrics* **1997,** *203* (1), 249-268.
50. Maeda, M.; Hattori, M.; Hotta, A.; Suzuki, I. Dielectric Studies on $CH_3NH_3PbX_3$ (X = Cl and Br) Single Cystals. *J. Phys. Soc. Jpn.* **1997,** *66* (5), 1508-1511.
51. Chen, Y.-F.; Tsai, Y.-T.; Bassani, D. M.; Hirsch, L. Experimental evidence of the anti-parallel arrangement of methylammonium ions in perovskites. *Appl. Phys. Lett* **2016,** *109* (21), 213504.
52. Ang, C.; Yu, Z.; Youn, H. J.; Randall, C. A.; Bhalla, A. S.; Cross, L. E.; Nino, J.; Lanagan, M. Low-temperature dielectric relaxation in the pyrochlore $(Bi_{3/4}Zn_{1/4})_2(Zn_{1/4}Ta_{3/4})_2O_7$ compound. *App. Phys. Lett.* **2002,** *80* (25), 4807-4809.
53. Noh, J. H.; Im, S. H.; Heo, J. H.; Mandal, T. N.; Seok, S. I. Chemical Management for Colorful, Efficient, and Stable Inorganic–Organic Hybrid Nanostructured Solar Cells. *Nano Lett.* **2013,** *13* (4), 1764-1769.
54. Stoumpos, C. C.; Malliakas, C. D.; Peters, J. A.; Liu, Z.; Sebastian, M.; Im, J.; Chasapis, T. C.; Wibowo, A. C.; Chung, D. Y.; Freeman, A. J.; Wessels, B. W.; Kanatzidis, M. G. Crystal Growth of the Perovskite Semiconductor $CsPbBr_3$: A New Material for High-Energy Radiation Detection. *Cryst. Growth Des.* **2013,** *13* (7), 2722-2727.
55. Ryu, S.; Noh, J. H.; Jeon, N. J.; Chan Kim, Y.; Yang, W. S.; Seo, J.; Seok, S. I. Voltage output of efficient perovskite solar cells with high open-circuit voltage and fill factor. *Energy Environ. Sci.* **2014,** *7* (8), 2614-2618.
56. Kulbak, M.; Cahen, D.; Hodes, G. How Important Is the Organic Part of Lead Halide Perovskite Photovoltaic Cells? Efficient $CsPbBr_3$ Cells. *J. Phys.Chem. Lett.* **2015,** *6* (13), 2452-2456.
57. Im, J. H.; Lee, C. R.; Lee, J. W.; Park, S. W.; Park, N. G. 6.5% Efficient Perovskite Quantum-Dot-Sensitized Solar Cell. *Nanoscale* **2011,** *3*, 4088-4093.
58. Blöchl, P. E. Projector augmented-wave method. *Phys.Rev. B* **1994,** *50* (24), 17953-17979.
59. Kresse, G.; Hafner, J. Ab initio molecular dynamics for liquid metals. *Phys. Rev.B* **1993,** *47* (1), 558-561.
60. Kresse, G.; Furthmüller, J. Efficient iterative schemes for ab initio total-energy calculations using a plane-wave basis set. *Phy. Rev. B* **1996,** *54* (16), 11169-11186.
61. Kresse, G.; Joubert, D. From ultrasoft pseudopotentials to the projector augmented-wave method. *Phys. Rev.B* **1999,** *59* (3), 1758-1775.
62. Perdew, J. P.; Ruzsinszky, A.; Csonka, G. I.; Vydrov, O. A.; Scuseria, G. E.; Constantin, L. A.; Zhou, X.; Burke, K. Restoring the Density-Gradient Expansion for Exchange in Solids and Surfaces. *Phys. Rev.Lett.* **2008,** *100* (13), 136406.
63. Allen, M. P., Tildesley, D. J. Computer simulation of liquids (Oxford university press, 1991).